Full-Field Pressure and Strain Measurement Technique Using a Dual-Layer Luminescent Coating

James P. Hubner,* Amruthkiran Hegde,† Kyle Chism,‡ and Semih M. Ölçmen*
University of Alabama, Tuscaloosa, Alabama 35487
and
Jim Crafton§
Innovative Scientific Solutions, Inc., Dayton, Ohio 45440

https://doi.org/10.2514/1.J060058

This paper reports on the combination of two surface measurement techniques, pressure-sensitive paints (PSPs) and photoelastic coatings (PECs), to measure full-field, dynamic pressure and strain fields. The technique applies a fast PSP onto the surface of a PEC adhered to the test specimen. A dual light-emitting diode approach is used to overcome poor polarization retention of the PSP luminophore. The theory of the technique is presented. Experiments and corresponding results on a vibrating cantilever beam specimen placed within a pressure chamber and driven near resonant frequency as well as on an inclined flap in supersonic flow demonstrate the feasibility and current limitations of the technique. Sensitivity and interference effects are discussed.

Nomenclature

A, B	=	pressure-sensitive paint calibration coefficients
a	=	coating absorptivity, 1/nm
E	=	modulus of elasticity, Pa
F, G	=	amplitude and phase of optical strain response
h	=	coating thickness, mm
I	=	emission intensity, e^- (electrons) or ADU (analog-to-digtial unit)
I_{ref}	=	reference emission intensity, e^- or ADU
K	=	photoelastic coating sensitivity
L	=	length of beam (clamp to free end), mm
N	=	fringe order
P	=	pressure, kPa
P_{ref}	=	reference pressure, kPa
T_g	=	glass transition temperature, °C
t	=	time, s
α	=	analyzer angle or flow reattachment angle, deg
β	=	oblique shock angle, deg
γ	=	maximum in-plane shear strain, $\mu\varepsilon$ (microstrain)
δ	=	flap angle, deg
ε_i	=	principal strains
θ	=	principal strain direction, deg
λ	=	wavelength, nm
λ^*	=	effective excitation-emission wavelength
λ_{em}	=	emission wavelength, nm
λ_{ex}	=	excitation wavelength, nm
λ^*	=	effective excitation-emission wavelength, nm
ν	=	Poisson ratio
σ	=	standard deviation
ϕ	=	polarization efficiency

Presented as Paper 2020-2969 at the AIAA Aviation Forum, Virtual, June 15–19, 2020; received 11 August 2020; revision received 4 October 2020; accepted for publication 8 October 2020; published online 30 November 2020.

*Professor, Aerospace Engineering and Mechanics. Associate Fellow AIAA.

†Graduate Research Assistant, Aerospace Engineering and Mechanics. Member AIAA.

‡Graduated Research Assistant; currently Research Engineer, Lockheed Martin, Denver, Colorado. Member AIAA.

§Senior Research Scientist and Vice President. Senior Member AIAA.

I. Introduction

VALIDATION of unsteady theoretical and computational fluid–structure interaction models for flight technologies and systems, particularly pressure fluctuations, requires high temporal and spatial resolution data and corresponding measurement techniques. Acquisition of these data is often compromised by traditional surface and off-surface probes that can interfere with and distort the airflow, necessitating correction techniques. Pointwise techniques such as pressure taps, accelerometers, and strain gauges, while highly accurate, can have insufficient spatial resolution or add time and cost to instrument the model. As such, full-field surface measurement techniques are of interest to the aerodynamic testing community.

This paper presents the progress towards integrating two full-field optical sensor techniques to measure the unsteady, distributed loads (pressure) and strains on aerodynamically induced vibrating or deforming surfaces, with the goal to extend into high-speed flows. The approach is to combine fast-response pressure-sensitive paints with thin photoelastic coatings to create a fast luminescent pressure and strain measurement technique. The average and variance of emission intensity across pixels sensitive to polarization state are hypothesized to track the pressure, P, and maximum in-plane shear strain, γ, respectively.

In this paper, progress in the development of the technique is presented. First, pressure and strain measurements of a cantilever beam specimen driven at frequencies to induce a dynamic stress/strain field are presented. The specimens are placed in a pressure-controlled environment. This is a continuation of prior benchtop testing and development of the technique [1]. Second, initial testing of the technique on an inclined flap in Mach 3 flow is presented. The long-term motivation of the research is to develop the technique to measure correlated dynamic pressure and strain fields arising from transient mechanical loads in high-speed flows due to phenomena such as flow separation or shock-wave/boundary-layer interactions.

II. Background and Theory

A. Pressure-Sensitive Paints

The pressure-sensitive paint (PSP) technique [2] has become a common measurement technique in the aerodynamic community, and successful implementations of fast pressure-sensitive paints have followed due to improvements in paint formulations, ultrabright light-emitting diodes (LEDs), and high-quantum-efficiency high-speed digital cameras. A typical PSP is composed of two parts: an oxygen-sensitive fluorescent molecule and an oxygen permeable binder. When a luminescent molecule absorbs a photon of appropriate wavelength, it transitions to an excited energy state. The molecule then typically recovers to the ground state by the emission of a longer-wavelength

photon (as there is a loss of energy due to thermal relaxation). In the presence of and interaction with oxygen, the higher-energy state of the luminophore can transition to the ground state nonradiatively; this process is known as oxygen quenching. The rate at which these two processes compete is dependent on the partial pressure of oxygen, with a higher oxygen pressure increasing the quenching of the molecule and decreasing the measured luminescence.

Image-based pressure measurements using PSP are accomplished by coating the model surface with the paint and illuminating the surface with light of the appropriate wavelength (usually in the UV to blue range) to excite the luminescent molecules within the coating. The surface is imaged through a bandpass or long-pass filter (LPF) to separate the luminescent signal from the excitation light. The luminescent signal from the paint is not only a function of pressure but also varies with illumination intensity, luminophore concentration, paint layer thickness, and detector sensitivity. These spatial variations result in a nonuniform intensity field from the painted surface. The spatial variations are usually eliminated by taking the ratio of the PSP luminescent intensity at an unknown test condition I and a known reference condition I_{ref}. Most PSPs are modeled following the linear Stern–Volmer relationship [2], as shown in Eq. (1):

$$\frac{I_{\text{ref}}}{I} = A + B\frac{P}{P_{\text{ref}}} \tag{1}$$

For Eq. (1), A and B are temperature-dependent coefficients and P is pressure. For more complicated quenching processes, other response models are used and include higher-order polynomials or nonlinear dual-sorption models.

Conventional PSP formulations typically use a polymer as the binder material. Polymer binders enable the diffusion of oxygen into the embedded dye molecules. The response time of the paint is largely governed by the rate of oxygen diffusion into the binder, enabling interaction with the luminophore. This is nominally proportional to the thickness squared and inversely proportional to the binder diffusivity. Thicker, conventional coatings have longer response times not suitable for dynamic measurements. Decreasing the coating thickness to improve response time has the disadvantage of sacrificing luminescent output and signal-to-noise ratio. Anodized aluminum and porous polymer PSPs increase response times, demonstrating bandwidths of 100 kHz; however, a drawback of anodize aluminum PSPs is nearly complete quenching at lower pressures (less than 20 kPa) compared to conventional or porous polymer PSPs, thus severely limiting their pressure range [3]. Hybrid paint formulations use ceramic particles in the paint, creating a porous structure that decreases the effective thickness, increases the effective diffusivity, and extends the pressure range. This results in a fast-response system with a favorable signal-to-noise ratio. Hybrid fast-PSP formulations can detect pressure fluctuations up to 20 kHz, and unsteady pressure measurements have been demonstrated on a variety of models [3–7]. The fast PSP has also been paired with stereophotogrammetry techniques to measure pressure and deformation [8].

B. Photoelastic Coatings

Photoelastic coatings (PECs) [9] have been used in the structural testing community for many years, primarily for static testing but applicable to dynamic testing related to stress wave propagation and impact [10]. The dynamic response of photoelastic coatings is high due to the propagation of wave speeds through the thin coatings. The typical PEC density and elastic modulus are approximately 1000 kg/m^3 and 1 GPa, respectively. Thus, for a 1-mm-thick coating, the theoretical response time based on wave propagation would be approximately 1 μs.

Photoelastic coatings work on the principle of birefringence: the ability of a material to transmit light at different velocities relative to the polarization and propagation of the incoming light. In application, a reflective photoelastic coating is adhered to the surface of the model and illuminated with circular polarized light [a combination of a linear polarizer (LP) and an achromatic quarter-wave plate (QWP) rotated 45 deg relative to the polarizer]. The stress-induced change in the polarization as light passes into and reflects out of the coating is measured using a second linear polarizer, often called an analyzer, and a camera. This configuration is sometimes referred to as a grayscale polariscope [11]. A more traditional configuration for PECs combines a quarter-wave plate and polarizer in front of the imager [9].

As with all birefringent coatings, the change in polarization is related to the maximum shear strain γ, in the plane perpendicular to the path of the polarized light passing through the specimen. To quantify the strain field, a sequence of images at different analyzer angles is necessary. The development of micropolarizer masks attached to the imager chip eliminates the need of an exterior rotating analyzer or polarimetric lens to capture multiple analyzer states with each image. The group of pixels with each polarization orientation, typically four, is called a superpixel.

The luminescent photoelastic coating (LPC) technique [12] consists of a luminescent dye in, on, or underneath a photoelastic binder. The luminescence creates a more uniform emission field at oblique incidence angles compared to the reflected field of traditional reflective photoelastic coatings. This higher relative signal on oblique surfaces enables the potential of principal strain separation [13]. The emission intensity of an LPC after it passes through the analyzer is characterized by Eq. (2) [12],

$$\frac{I_\alpha}{\bar{I}} = 1 + F\sin(2\alpha - 2G) \tag{2}$$

where I_α is the pixel intensity for a specific analyzer orientation, $\bar{I}$ is the average measured emission intensity over all the analyzer states (usually four), α is the analyzer angle, F is the magnitude of the optical strain response (OSR), and G is the phase of the OSR. The phase is related to the principal strain direction relative to the designated 0 deg analyzer (or pixel) angle of the camera. The OSR is a function of the in-plane maximum shear strain γ. For a single-layer LPC with both a luminescent dye for strain detection and an absorption dye for thickness independence [12], the OSR is

$$F = \phi\frac{\gamma/\eta}{1 + (\gamma/\eta)^2} \quad \text{and} \quad \eta = \frac{a\lambda^*}{2\pi K} \tag{3}$$

where ϕ is the polarization-retention efficiency of the luminescence and η is the coating characteristic, which is a function of the dye absorptivity a, the coating optical sensitivity K, and the effective excitation-emission wavelength λ^*:

$$\lambda^* = \frac{\lambda_{\text{ex}}\lambda_{\text{em}}}{\lambda_{\text{ex}} + \lambda_{\text{em}}} \tag{4}$$

The polarization efficiency depends on the ability of the luminescent process to retain the state of excitation polarization after emission. The optical sensitivity is a material property of the coating and is generally higher for epoxy- or polycarbonate-type materials [9]. If there is no absorption dye in the coating, the measured luminescent intensity increases and the OSR is [14]

$$F = \phi\frac{1 - \cos(\gamma/\eta)}{\gamma/\eta} \quad \text{and} \quad \eta = \frac{\lambda^*}{2\pi hK} \tag{5}$$

where h is the thickness of the coating. This approach increases signal output and the expense of being thickness dependent. Finally, a dual-layer (DL) coating with a single-LED excitation source places the luminescent dye above the PEC ($\lambda^* = \lambda_{\text{em}}/2$, double pass emission through the coating) or below the PEC [$\lambda^* =$ Eq. (4)]. For these two cases, the polarized emission intensity is

$$F = \phi\sin\left(\frac{\gamma}{\eta}\right), \qquad \eta = \frac{\lambda^*}{2\pi hK} \tag{6}$$

Figure 1 compares the theoretical OSR for the coating with an absorption dye, without absorption dye, and with the luminescent dye above the coating assuming $\phi = 1$. The polarization efficiency and

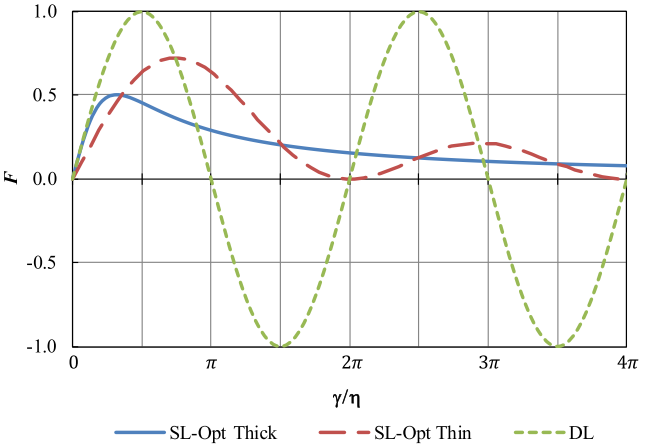

Fig. 1 Optical (Opt) strain response *F* of a single-layer (SL) coating with absorption dye [solid line; Eq. (3)], single-layer coating without absorption dye [dashed line; Eq. (5)], and dual-layer coating [dotted line; Eq. (6)].

coating characteristic are determined through *in situ* or *a priori* calibration. Whereas the latter is easier to implement if known, the former is more accurate, assisting in the elimination of systematic errors that can arise from batch variance, surface reflectance, optical interference, and environmental dependencies. The retention of polarization during the luminescence process depends on the type of luminophore and its concentration, and the corresponding polarization efficiency will be less than one.

The coating characteristic η, can be thought of as a characteristic strain value that affects the range and sensitivity of the strain response. As the coating characteristic increases, the strain to achieve the first peak in Fig. 1 ($\gamma/\eta = \pi/2$ for the DL case) increases. Given a set bit resolution of the camera, this will decrease the effective strain sensitivity. For strain values beyond the first OSR peak ($\gamma \geq \eta\pi/2$), the relationship is multivalued, and thus requires fringe counting and phase-unwrapping techniques. For this investigation, $\gamma/\eta < \pi/2$. There are potentially multiple approaches to extend the strain range: decrease the coating thickness, use a PEC with lower optical sensitivity K, or increase the effective wavelength. The latter approach would be the most difficult because it depends on the absorption and emission properties of the luminescent coating.

C. Combined Technique

The initial approach to combine the two techniques was to use a DL coating with a single-LED excitation source (Fig. 2a). The luminescence of the PSP (top layer) would pass through the PEC (bottom layer) [1]. The DL coating would be excited by an appropriately matched LED with LP/QWP optics. Pressure changes would quench the PSP emission, and strain changes would alter the emission polarization as it passed through the PEC and reflected off the surface toward the imager.

The response is modeled by assuming the strain information is carried in the polarization change of the emission and the pressure information is carried in the average intensity change of the emission. Correspondingly, the average of a superpixel would be strain independent based on the sinusoidal form of Eq. (2): assuming an even number of analyzer angles appropriately oriented. For a superpixel with four analyzer states of 0/45/90/135 deg,

$$\bar{I} = \frac{\Sigma I_\alpha}{4} \neq f(\gamma) \tag{7}$$

where I_α is the intensity of each pixel for $\alpha = 0/45/90/135$ deg. In terms of the pressure response, $\bar{I}$ is the effective superpixel intensity; thus,

$$\frac{\overline{I_{\text{ref}}}}{\bar{I}} = A + B\frac{P}{P_{\text{ref}}} \tag{8}$$

Substituting Eq. (8) into Eq. (2) for a dual-layer coating yields

$$\frac{I_\alpha}{\overline{I_{\text{ref}}}} = \frac{1}{A + B(P/P_{\text{ref}})}\left(1 + \phi \sin\left(\frac{\gamma}{\eta}\right)\sin(2\alpha - 2G)\right) \tag{9}$$

where $\overline{I_{\text{ref}}}$ is the unloaded, reference pressure state for a superpixel. Equation (9) is a sinusoid function with a relative intensity offset and amplitude equal to

$$\left(\frac{I_\alpha}{\overline{I_{\text{ref}}}}\right)_{\text{avg}} = \frac{1}{A + B(P/P_{\text{ref}})} \tag{10a}$$

and

$$\left(\frac{I_\alpha}{\overline{I_{\text{ref}}}}\right)_{\text{amp}} = \frac{\phi \sin(\gamma/\eta)}{A + B(P/P_{\text{ref}})} \tag{10b}$$

respectively. Theoretically, each superpixel represents a pressure and strain state on the model surface.

This approach requires the PSP coating luminescence to partially retain the polarization of the excitation to be able to detect the strain-induced birefringence. The advantage of this approach is a single excitation source. The efficiency of polarization retention for the PSP luminophore, however, proved to be low compared to luminophores designed for LPCs that do not require oxygen quenching, resulting in poor strain resolution and long exposure times (greater than 100 ms) [1].

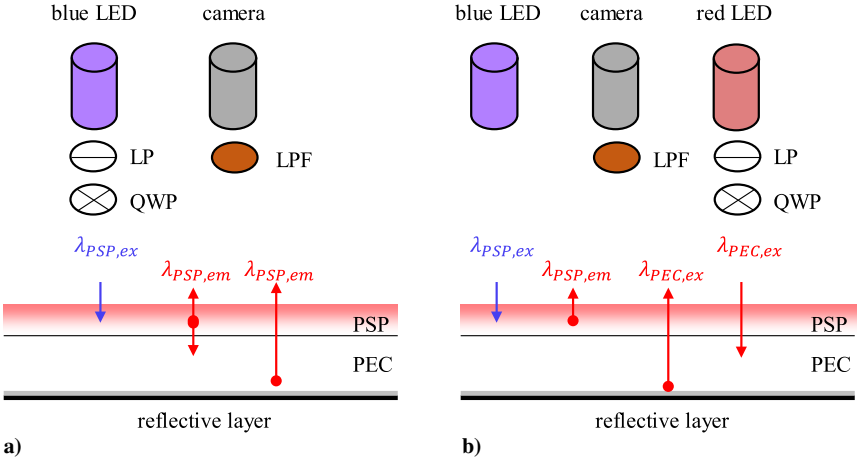

Fig. 2 Schematic of one- and two-LED coating excitation approaches; the red/blue LED approach (Fig. 2b) uses alternating strobed pulses.

Thus, an alternative method is a two-LED approach (Fig. 2b): a blue LED without polarization optics used to excite the PSP (pressure response), and a red LED with polarization optics (LP/QWP pair) used to detect stress-induced polarization of the PEC (strain response). The blue and red LEDs are strobed out of phase with each other. The main costs of the two-LED approach are alternating pressure and strain measurements (images). This downside, though, is outweighed by a strong strain-dependent signal and faster acquisition rates afforded by pairing the polarization optics on the red LED. Because the PEC response is based on light reflection as opposed to the PSP emission, where intensity and polarization are affected, the PEC requires a less powerful LED. Thus, it is preferred to pair the polarization optics on the red LED.

Figure 3 is a schematic of the two LED approach implemented for a vibrating beam test. The PSP is applied on top of the PEC but not at thickness or concentration to block the red LED excitation into the PEC. Further discussion of the PEC and PSP application is in Sec. III. The camera and two LEDs are triggered with an external source. The camera is triggered at twice the frequency of the LEDs. The LEDs are triggered 180 deg out of phase with each other, and their duty cycle is less than 50% to synchronize with the camera exposure time. An LPF blocks the blue LED excitation and allows the PSP emission and the PEC reflection to pass through to the imager. The light is imaged through a pixilated polarizer mask on the digital camera. Each pixel measures an intensity relative to the polarization orientation of that pixel. A typical micropolarizer array has four discrete orientations in a 2×2 pattern: 0/45/90/135 deg.

The PSP emission and PEC reflection intensities recorded by each pixel are dependent on pressure, strain, excitation intensity, and coating thickness/concentration. Like the single-LED approach, the pressure information is tracked by the average of the four pixel intensities (assuming strain independence), and the strain information is modeled by the variance of the pixel intensities (assuming pressure independence). For a superpixel exposed to the blue LED (pressure signal),

$$\overline{I_b} = \frac{\Sigma I_{b,\alpha}}{4} \tag{11}$$

In terms of the Stern–Volmer pressure response,

$$\frac{\overline{I_{b,\text{ref}}}}{\overline{I_b}} = A + B\frac{P}{P_{\text{ref}}} \tag{12}$$

The strain response for the two-layer coating exposed to the red LED is modeled by

$$\frac{I_{r,\alpha}}{\overline{I_{r,\alpha}}} = 1 + \sin\left(\frac{\gamma}{\eta}\right)\sin(2\alpha - 2G) \tag{13}$$

Polarization efficiency is assumed to be $\phi = 1$ because the PEC response is not based on PSP luminescence but instead on reflection of the polarized red LED illumination. Relative to the pixel orientation α, the measured intensity follows a sinusoidal curve $\sin(2\alpha - 2G)$. The amplitude of the corresponding curve fit, or the OSR, is $\sin(\gamma/\eta)$. The variance across the four pixels is referenced to the average intensity of the four pixels, $\overline{I_{r,\alpha}}$. To calculate the OSR and the phase, and hence the strain and principal direction, a nonlinear fit algorithm such as the Levenberg–Marquardt routine is suitable. Alternatively, and more computationally efficient, the standard deviation of $I_{r,\alpha}/\overline{I_{r,\alpha}}$ for a superpixel can be used:

$$\text{OSR} = \sin\left(\frac{\gamma}{\eta}\right) = \sqrt{\frac{2(n-1)}{n}}\,\text{stdev}\left(\frac{I_{r,\alpha}}{\overline{I_{r,\alpha}}}\right) \tag{14}$$

where n is the number of evenly spaced pixel orientations (in this case, $n = 4$). To calculate the phase,

$$2G = \text{atan2}\left(\frac{I_0 - I_{90}}{I_{45} - I_{135}}\right) \tag{15}$$

In cases where the strain is zero or at a fringe node, the intensity ratio is constant with respect to analyzer orientation and OSR $= 0$. If the OSR is not zero at the reference no-load state (e.g., a residual or parasitic birefringence in the coating), then a vector subtraction of the residual state is necessary [15]. This is discussed further in Sec. IV.D.

When calculating the corresponding strain from the measured OSR, multiple strain values could result. This requires fringe counting or phase unwrapping. By limiting the coating thickness to less than a quarter-fringe for the expected strain range, the fringe counting is eliminated. The fringe order N, is

$$N = \frac{\gamma}{2\pi\eta} \tag{16}$$

This corresponds to $N < (1/4)$ or $\gamma_{\max} < (\lambda^*/4hK)$.

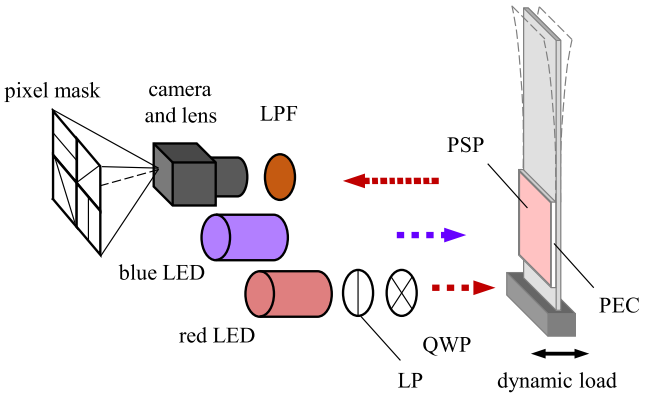

Fig. 3 Schematic of the dual-LED/single-camera configuration; the red and blue LEDs are pulsed out of phase with each other.

III. Benchtop Test Apparatus

Figure 4a is an image of the benchtop pressure and shake chamber used in this investigation. To excite the PSP, an air-cooled Innovative Scientific Solutions, Inc. (ISSI) LM3X 400 nm (blue) 36 W LED lamp is used. To illuminate the PEC, an ISSI LM2 620 nm (red) 4 W LED lamp is used. Aligned in the red LED excitation path is a linear polarizer and an aachromatic QWP, rotated at 45 deg relative to the polarizer, to create circular polarized red light. The imager is a 4D-Technologies PolarCam U2 Complementary metal-oxide-semiconductor (CMOS) camera with a 0/45/90/135 deg wire-grid polarization mask. The wire-grid polarizer is suitable for a broad wavelength spectrum, with a transmission ratio greater than 80% for wavelengths above 450 nm. The maximum full-field frame rate is 164 frames per second (fps) at 12- bits, but higher frames rates are possible for smaller and rotated regions of interest. Attached to the camera is a Nikon 50 mm lens set at an f-stop of 1.2. A 450 nm reflective LPF and 570 nm Schott glass LPF are attached to the lens.

National Instruments data acquisition hardware is used to trigger the LEDs and camera, as well as record calibrating strain gauge measurements (NI-9237 and NI-9263 modules, respectively). The LEDs are triggered alternatively at half the rate of the camera and a 45% duty cycle. This enables the camera to alternatively capture pressure (blue) and strain (red) signals. Triggering and strain gauge recording are performed with in-house LabVIEW virtual instruments. PolarCam software [16], provided by 4D Technologies, is used to control the camera when focusing the image, establishing appropriate exposure times and tuning (rotating) the QWP to create circular polarized excitation. Also, *eBus Player* software is used to set parameters in trigger mode and control the camera while externally triggering.

The specimens are thin aluminum (6061-T6) cantilever beams. The pressure and shake chamber (Fig. 4a) can accommodate specimens 1–3 mm thick, 20–30 mm wide, and up to 260 mm long. The chamber pressure range is 10 to 101 kPa absolute. A glass window was designed and fabricated to replace a thicker acrylic window that

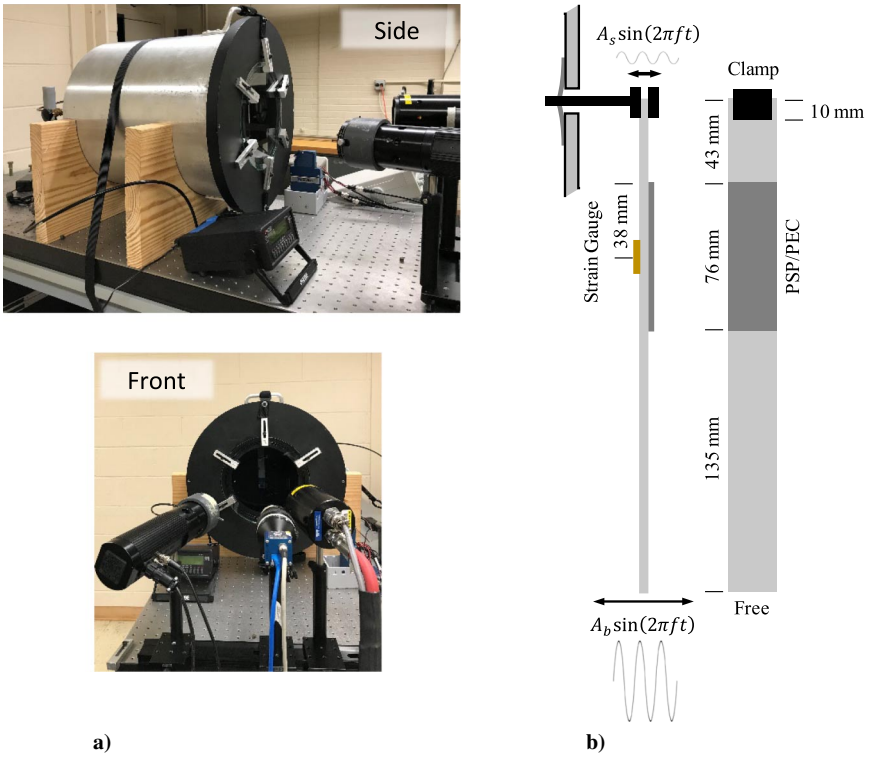

Fig. 4 PSP/PEC test apparatus (Fig. 4a) and dimensions of the beam specimen (Fig. 4b).

was initially used with the chamber. The glass window decreases the photoelastic interference created when the window is stressed by subatmospheric pressure.

For this investigation, specimens are 25.4×254 mm. The results for a 2.3-mm-thick beam are presented in the next section. The beam was clamped at one end and sinusoidally driven using a shaker rod passing through the chamber's backside and connecting to the beam mount (Fig. 4b). The shaker frequency and amplitude are set by an external function generator and preamplifier. Strain amplification is achieved by driving the specimen near resonance. Due to inertial acceleration, the induced stress in the cantilever specimen will decrease from the base to the free end. The principal stress aligns along the length of the beam, and the corresponding maximum in-plane shear strain is $\gamma = \varepsilon_1 - \varepsilon_2 = (1 + \nu)\varepsilon_1$.

A 76×25.4 mm strip of PEC (Micro-Measurement PS-1; $h = 0.51$ mm, $K = 0.15$) was adhered with PC-10 reflective adhesive near the clamped end of the specimen. Next, the PSP was sprayed on the surface of the PEC. First, a water-based polymer formulation was sprayed onto the PEC. This underlayer assists in protecting the PEC from the solvents of the PSP layer. The polymer included a small volume of a low refraction index porous media instead of traditionally used titanium dioxide because the latter affected polarization. Then, a thin layer of Platinum meso-tetrakis(pentafluorophenyl) porphine (PtTFPP) PSP [7] was sprayed on the surface of the polymer until a light-pink hue of the PSP was visible, balancing between the signal strength of the PSP (more is better for the emission from the blue LED) and the PEC (less is better for the reflection from the red LED). The pressure response time in a calibration shock tube at ISSI was measured at 2 ms. The center absorption band of the PSP is approximately 400 nm, and the center emission band is near 650 nm. Thin layering of the PSP allows 620 nm excitation of the red LED to pass through the PEC. The theoretical coating characteristic η is 645 $\mu\varepsilon$. A uniaxial electrical resistive strain gauge aligned with the length of the beam was adhered to the back side of the specimen to record the time-dependent maximum principal strain profile.

IV. Results and Discussion

The beam specimen was excited sinusoidally at 23.5 Hz, which is lower than the fundamental frequency, to limit the maximum induced strain. The camera was triggered at 200 Hz. The pixel density was 5.9/mm. Data were acquired at four chamber pressure ratios: 0.20, 0.41, 0.61, and 1.00. Image postprocessing included flat-field correction, dark image correction, four-point affine image registration, median-filter smoothing, and parasitic (zero-load) OSR correction. The effects of registration and filtering on a pressure ratio image, and subsequent improvements, are shown in Fig. 5.

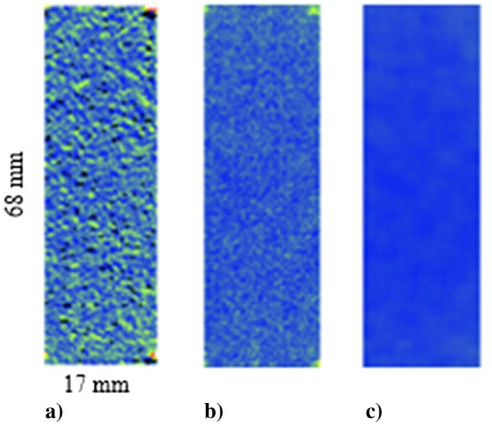

Fig. 5 Intensity ratio contour for $P/P_{\text{ref}} = 0.2$: a) no registration, b) with registration, and c) with registration and smoothing.

A. Pressure Response

Figure 6 is a plot of the intensity ratio $\overline{I_{b,\text{ref}}}/\overline{I_b}$, the OSR and the phase recorded with unpolarized blue LED excitation at $P/P_{\text{ref}} = 0.20$. The reference state is atmospheric pressure and at rest (i.e., no load). Images from left to right represent time steps of 10 ms. The intensity ratio (top row; proportional to the average of the superpixel) is approximately constant across the field of view ($\overline{I_{b,\text{ref}}}/\overline{I_b} = 0.33$), showing no measurable strain interference or pressure changes due to the oscillation. The OSR (middle row; proportional to the standard deviation of the superpixel relative to the average of the superpixel) is near zero as expected because the

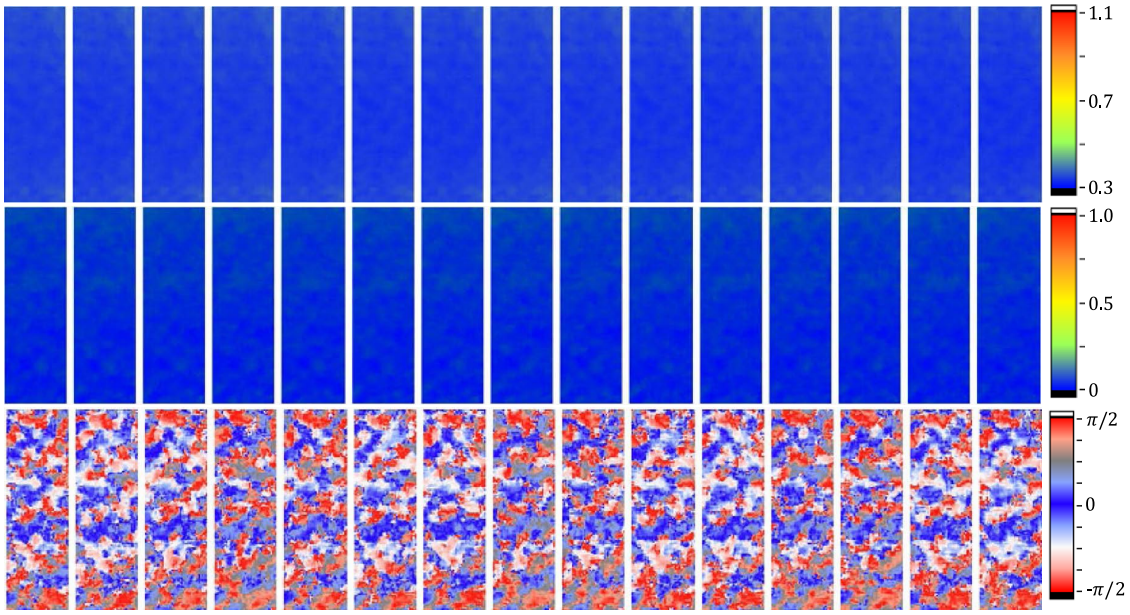

Fig. 6 Intensity ratio $\overline{I_{b,\mathrm{ref}}}/\overline{I_b}$ (top row), OSR (middle row), and phase G (bottom row; in radians) recorded for the unpolarized blue LED excitation at $P/P_{\mathrm{ref}} = 0.20$: beam driven at 23.5 Hz; images from left to right represent time steps of 10 ms.

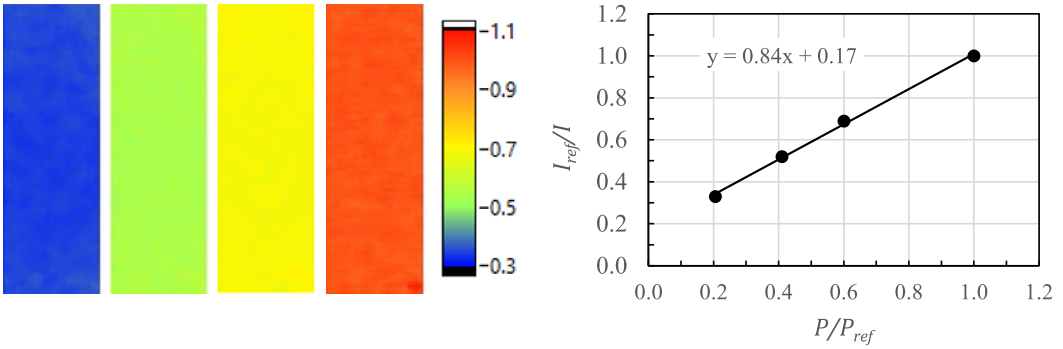

Fig. 7 Intensity ratio contour (left) for $P/P_{\mathrm{ref}} = 0.20$, 0.41, 0.61, and 1.00; and corresponding Stern–Volmer plot (right) for blue LED excitation.

blue LED excitation is unpolarized; thus, the measured intensities of the four pixels are approximately equal. The phase plot (bottom row; indication of principal strain direction) is scattered, ranging between 0 and $\pm\pi/2$. This is also a result of the unpolarized excitation. The difference in pixel intensity is small, leading to large variations resulting from Eq. (15). The splotchy nature of the phase plot is a remnant of the median filter kernel size. Thus, the information of interest from the blue LED excitation is only the intensity ratio: $\overline{I_{b,\mathrm{ref}}}/\overline{I_b}$. Figure 7 (left) compares the intensity ratio at four different pressure ratios. Figure 7 (right) is the corresponding Stern–Volmer plot.

B. Strain Response

Figure 8 is a plot of the intensity ratio $\overline{I_{r,\mathrm{ref}}}/\overline{I_r}$, the OSR, and the phase recorded with polarized red LED excitation at $P/P_{\mathrm{ref}} = 0.41$. Again, the reference state is atmospheric pressure and at rest. Images from left to right represent time steps of 10 ms. The intensity ratio (top row) varies relative to time and location. Unlike the previously shown luminescence process of the PSP due to the blue LED excitation, the PEC is a reflection-base measurement using the red LED. Thus, as the beam moves back and forth, changing its proximity and surface orientation relative to the camera, varying light intensity is recorded by the camera. The strain information, though, is not recorded in the average of the superpixel intensity but instead the relative variation in the superpixel intensity to the average superpixel intensity [Eq. (13)]. This is plotted in the middle row where the OSR indicates a change in the maximum shear strain from image to image (as the beam vibrates). As oriented in the image, the beam is clamped at the top, and the free end is at the bottom. As the beam is driven by the shaker, the region near the clamped end exhibits a higher OSR (or strain) than the free end. The phase plot (bottom row) correlates with the OSR images. As the beam vibrates, the surface is alternating between states of tension and compression. The camera is mounted such that the pixel with the designated 0 deg polarization orientation is aligned with the length of the beam. This enables the ability to reference the measured principal strain direction to the specimen coordinate system. For this simple beam configuration, when the phase measures 0 deg, the side of the beam facing the camera is in tension. And, when the phase measures $\pm\pi/2$, the side of the beam facing the camera is in compression. As the beam transitions between tension and compression, the corresponding OSR response transitions between 0 deg (blue) and $\pm\pi/2$ (red). At instances of low strain, the phase plots indicate the onset of transition between tension and compression (white and gray tones).

At the LED trigger rate, about four images are captured per beam oscillation (tension–compression cycle). Figure 9 is a plot of the OSR at the circle locations indicated in Fig. 8. Overlaid on the OSR measurements is a rectified sinusoidal fit to the experimental data, indicating the time-dependent OSR. The OSR is related to the maximum shear strain (the diameter of the Mohr circle) via Eq. (14). Peaks alternate between tension and compression as indicated by the phase value in Fig. 8. Based on the fit in Fig. 9, the peak relative strain, γ/η, per cycle is calculated. Due to coating reinforcement, the PEC fringe order must be corrected for PEC reinforcement (stiffening) and thickness gradient effects [15]. These effects become a greater factor as the ratio of coating-to-specimen thickness or modulus of elasticity

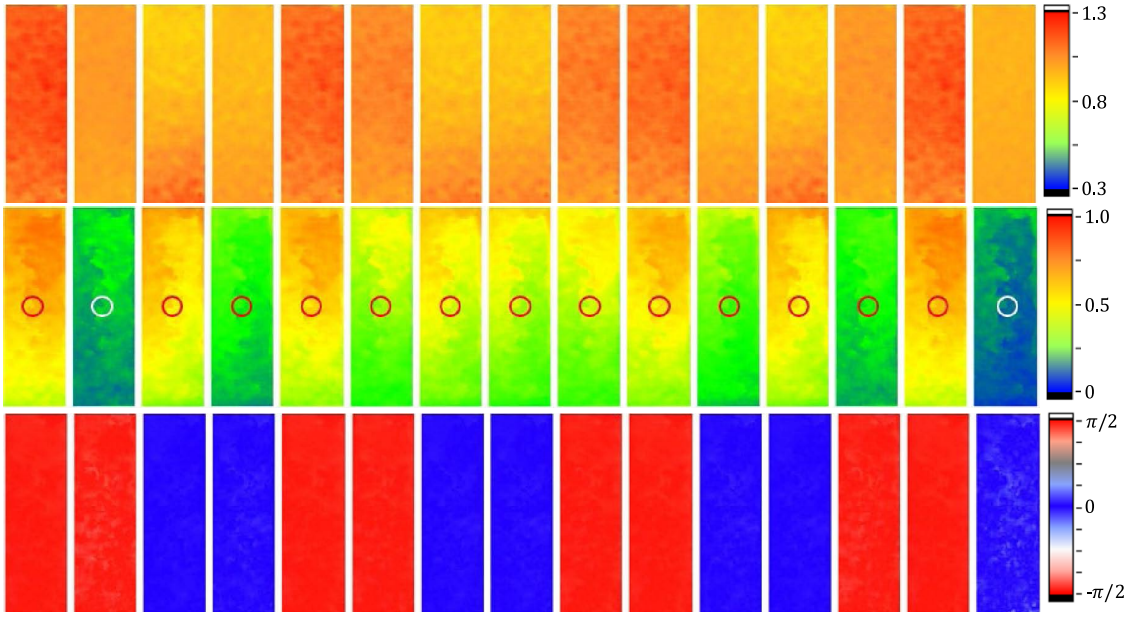

Fig. 8 Intensity ratio $\overline{I_{r,\mathrm{ref}}}/\overline{I_r}$ (top row), OSR (middle row), and phase G (bottom row; in radians) recorded for the polarized red LED excitation at $P/P_{\mathrm{ref}} = 0.41$: beam driven at 23.5 Hz; images from left to right represent time steps of 10 ms.

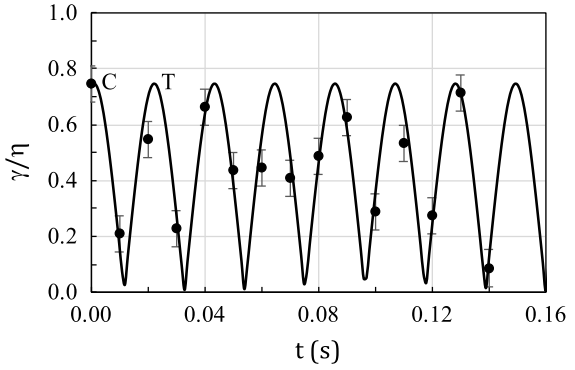

Fig. 9 Rectified sinusoidal fit (line) to the measured relative strain (γ/η, symbols): $P/P_{\mathrm{ref}} = 0.41$.

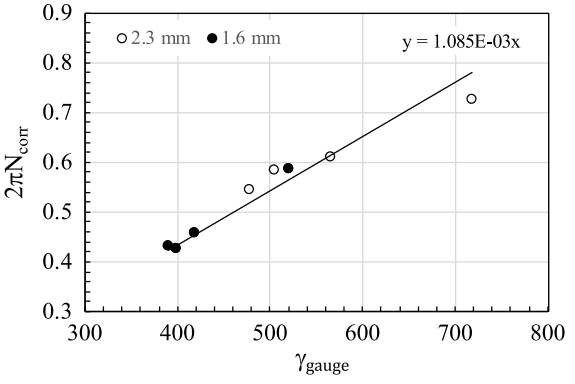

Fig. 10 Corrected fringe order calibration of the PEC with respect to the strain gauge reading (microstrain).

increases. For the thickness ratio and material properties of this test, $N_{\mathrm{corr}} = 0.86$ N. Figure 10 is an *in situ* calibration plot of the corrected fringe order for both the thick and thin (1.6 mm) specimens relative to the strain gauge reading (in microstrain). The slope inverse of this curve, 913, is η. This value is larger than the predicted *a priori* value of 645, indicating an interference or overestimation of a system parameter such as the coating sensitivity K. Finally, Fig. 11 is a plot of the relative strain along the length of the beam at various positions in the cycle.

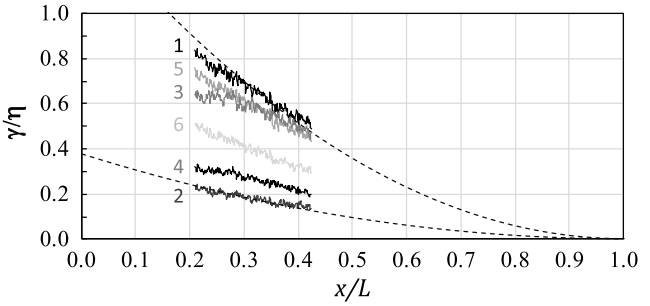

Fig. 11 Relative strain along the beam for the first six measurements of Fig. 8; dashed lines represent theoretical strain assuming no phase lag or damping.

As expected, the strain decreases from the clamped end toward the free end due to the inertial loading of the vibrating specimen. Similar pressure and strain results were recorded for the thinner beam [17].

C. Application

The first application in an aerodynamic test environment was performed in the University of Alabama Mach 3 supersonic wind tunnel (76 × 76 mm test section). The tunnel has a 108-mm-diameter window on the sidewall. A generic flap (Fig. 12) was designed and

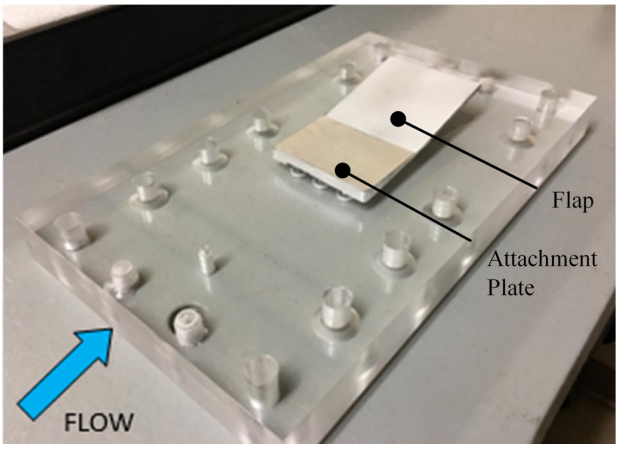

Fig. 12 Sidewall and installed surface flap (uncoated).

fabricated to install into the sidewall across from the window. Different-sized sidewall attachment plates allow flaps of various thicknesses, as well as resulting deformations due to the flow, to be installed. Each flap extends into the flow at an angle of 12 deg. The upstream surface length is 60 mm for both flaps. Due to the incline and different flap thicknesses, the down downstream lengths are 53 and 45 mm for the 1.6 and 3.2 mm flaps, respectively. The flap width is 57 mm (less than the width of the tunnel), generating a three-dimensional (3-D) flowfield. A schematic of the flowfield along the centerline of a rigid flap is shown in Fig. 13. Further details about the flap design are discussed in Ref. [17].

Figure 14 shows time-dependent pressure and strain results for two flaps, 1.6 mm thick and 3.2 mm thick, during flow startup. For each flap, the PEC (Micro-Measurement's PS-1; $h = 0.51$ mm) was adhered to the windward surface of the flap. The attachment plate was designed to account for the PEC thickness. The PSP polymer was sprayed on top of the PEC, followed by the luminescent dye. The two LEDs were strobed at 71 Hz with a 45% duty cycle and were 180 deg out of phase with each other. The camera was triggered at 142 Hz, limited by the PSP emission intensity at reference (room) conditions. While several hundred images were acquired, Fig. 14 only shows individual processed images capturing the startup flow event (time increasing from left to right at 14 ms increments). The top two rows are pressure contours, and the bottom two rows are strain contours. The first five to six pressure images on the left show a pressure drop as the butterfly valve fully opens. A low level of strain at the base of the thin flap is also present on the strain images. By the seventh image from the left, the shock structure is effectively set. The pressure profiles indicate a flow asymmetry in the test configuration, possibly due to the attachment plate or a sidewall interference, with a stronger pressure rise along the upper part of the flap. Due to the finite width of the flap and the 3-D nature of the flow, the pressure is lower along the side and the trailing edge of the flap. The thin flap, as expected, experiences higher strain, indicating a larger deformation. This in turn causes some pressure relief at the trailing-edge corners of the thin flap compared to the thicker flap. Some edge anomalies are present along the left edge of the thin flap due to localized coating damage.

D. Sensitivity and Corrections

In this section, further discussion is presented regarding camera noise, fringe reference correction, coating reinforcement, temperature dependence, and temporal response of the measurement technique.

1. *Camera Noise*

As with any measurement technique that uses digital cameras, shot noise, read noise, and dark noise can be important factors. The camera used in this experiment has a full-well capacity (FWC) of 33 ke^- (kilo-electron) and a 12-bit dynamic range. Intensity values are recorded as 16-bit (2 byte) integer tiff files. There is an effective tradeoff between the frame rate and camera noise because faster framing rates result in lower image intensities and higher relative shot noise unless additional excitation energy or pixel averaging is used. The frame rate, camera noise, and the expected intensity range (to avoid pixel saturation) should be considered when determining the exposure time. For this study, more emphasis was placed on higher framing rates, thus pressure reference images (high pressure, no load) were relatively low intensity: ~3% FWC. At low pressures and high strains expected during nominal test conditions, maximum intensities were estimated to be ~10% FWC, which were far from saturation.

At low intensity levels, the relative shot noise becomes most important. At 3% FWC, the relative shot noise is 4.6% for a ratio of two images at similar conditions. Because the pressure and strain measurement analysis uses four pixel orientations, the noise effectively decreases by $1/\sqrt{n}$ to 2.3%. This value was confirmed when analyzing images ratioed at atmospheric conditions. Based on the pressure and strain sensitivities of the coatings, this corresponds to a ~3–4% precision error in pressure and strain. As with precision

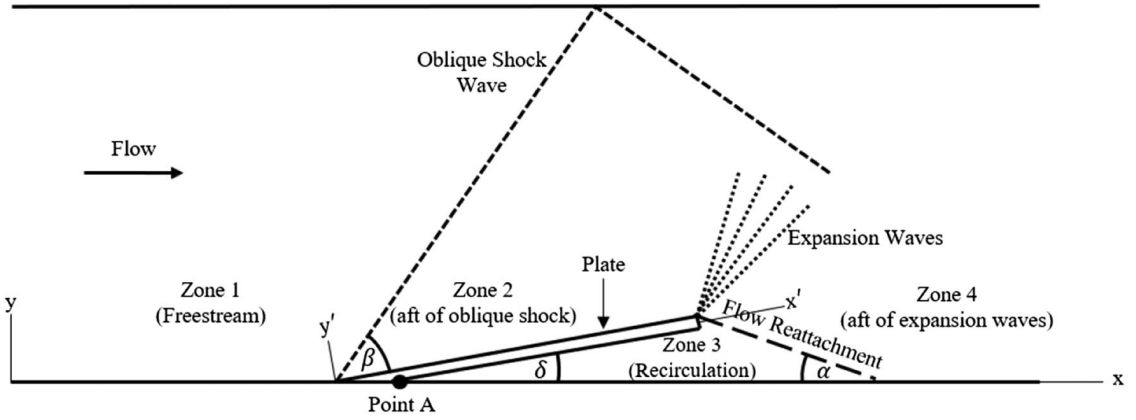

Fig. 13 Schematic of the flow environment along the flap centerline.

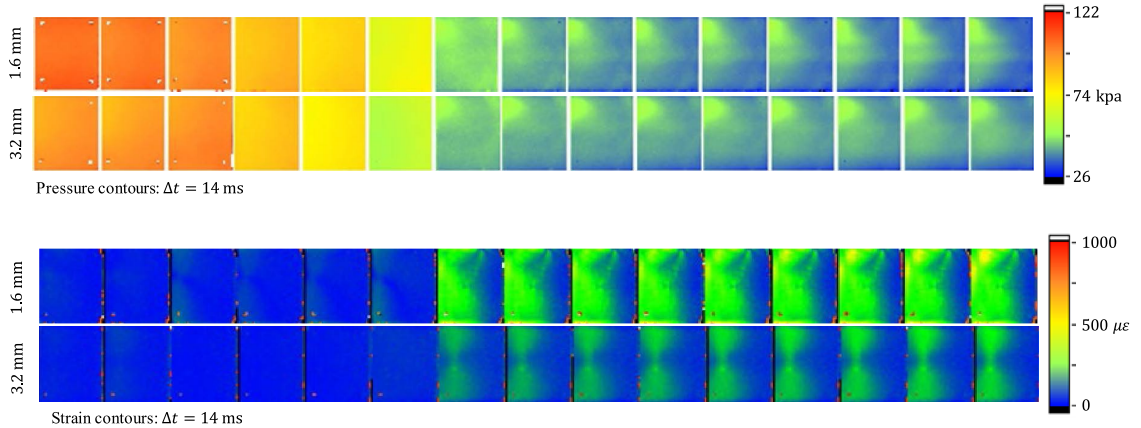

Fig. 14 Time-dependent pressure (top) and strain (bottom) on a 12 deg flap during tunnel startup: time step = 14 ms.

errors, this can be reduced with increased use of the imager FWC (more excitation or longer integration times) or pixel binning (at the expense of spatial resolution).

2. *Fringe Reference Correction*

Traditionally, the reference correction for the intensity-ratio approach of PSP measurements is performed by taking the ratio of the test (wind-on) image to a reference (wind-off, often atmospheric pressure) image. This assists in correcting for luminophore concentration, illumination level, and coating thickness [2]. With PECs, the reference state is generally an unloaded state (no applied load to induce a stress field). However, a nonzero OSR may be detected at the reference state due to the coating application, the age of the coating, a stress-induced state at the reference condition (for example, the weight of the specimen inducing a load or thermal difference between application and testing), or the extent the excitation is not circular polarized. This is referred to as parasitic or residual birefringence [15]. This is not to be confused with a residual stress that might exist in the specimen prior to coating application. A PEC would not detect a preexisting residual strain unless somehow the specimen was unloaded after the PEC was applied and in a manner without damaging the PEC.

If a nonzero (above the noise resolution) OSR exists for the reference case, then it can be corrected by treating the load and reference states as vectors and subtracting the reference state from the load state. First, similar to PSP image registration, the PEC wind-on images would be registered to the wind-off image. Next, the residual state would be corrected with a vector subtraction technique. A PEC measures the maximum shear strain γ (in the plane perpendicular to light propagation) and the principal strain direction G. Like the Mohr circle, the state of strain in terms of the fringe order [Eq. (16)] can be thought of as a vector with a magnitude equal to the fringe order and an angle equal to $2G$. As shown in Fig. 15a, N_{ref} and N_{meas} represent the two states captured by the camera: ref = without load and meas = with load. The measured fringe order N_{meas} includes both the effects of the reference state (an interference) and the applied state. The vector difference between N_{meas} and N_{ref} yields N_{app}. If the sum of the reference state and the applied load extend beyond the quarter-fringe boundary (Fig. 15b), then N_{meas} effectively rotates by π- rad, inducing an error where N'_{app} is an alias measure that is less than the applied value N_{app}.

Figure 16 plots the relative strain error, γ/η, and phase error G (in radians) when a 5% parasitic bias exists ($N_{\text{ref}} = 0.0125$, $G_{\text{ref}} = 0$) but is not corrected. This uncorrected bias results in up to a $\pm 8\%$ error in the strain, depending on the applied load magnitude and orientation, thus demonstrating the importance for fringe reference correction. As the applied load increases above the quarter-fringe value (range), the error significantly amplifies (black region of the scale). This would require phase-unwrapping techniques to correct, signifying the importance of coating thickness selection to set the range.

3. *Specimen Reinforcement*

As mentioned in Sec. IV.B, photoelastic coatings can induce a reinforcement effect on specimens. The load applied to the specimen is partially resisted by the coating, effecting the measured strain value and dynamic response. The resulting strain measurement is a function of coating-to-specimen thickness ratio, the coating-to-specimen

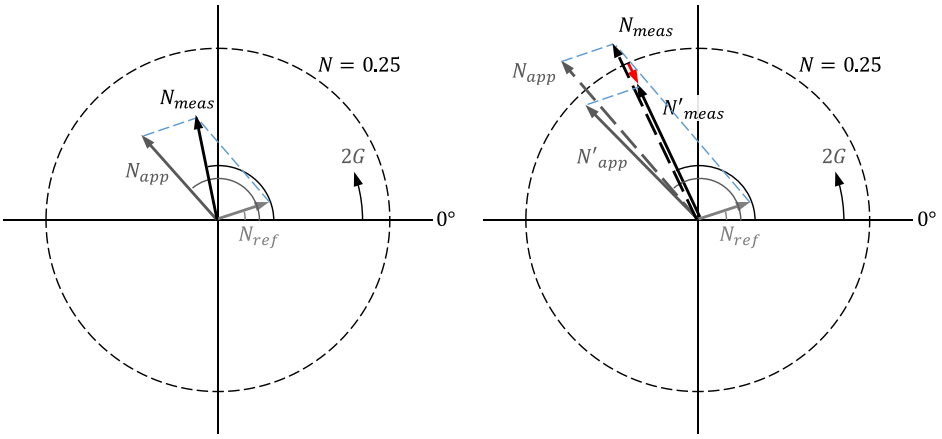

Fig. 15 Schematic showing relationship between reference (without load), measured (with load), and applied (true load) states for a PEC when the applied load is within the quarter-fringe boundary (left) and when it exceeds the quarter-fringe boundary (right).

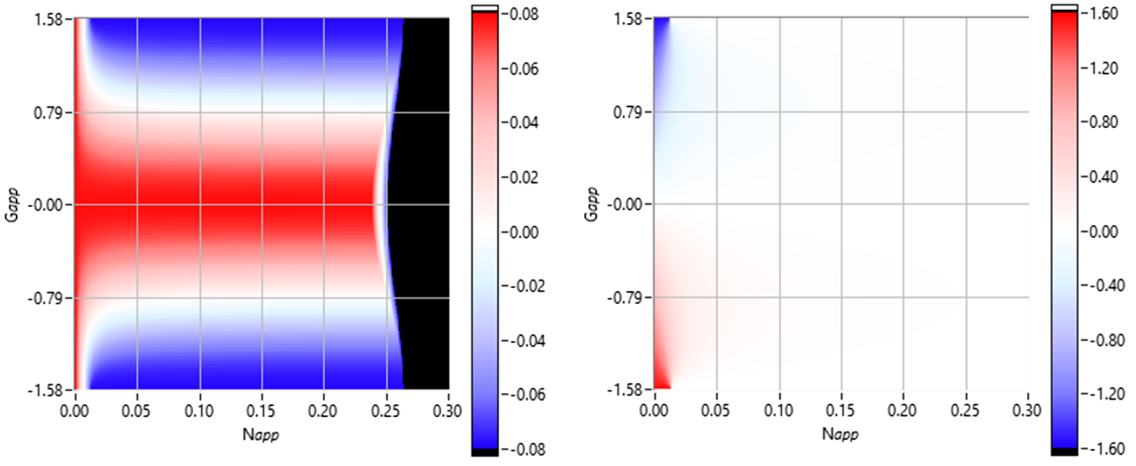

Fig. 16 Contours depict the relative strain error, γ/η (left), and phase error (G, in radians; right) when a 5% parasitic bias is not corrected from the measured fringe values.

modulus of the elasticity ratio, and the type of load (in- or out-of-plane deformation) [15]. Typically, the reinforcement effect is small if applied to metal specimens ($E_{\text{coating}} = 2.5$ GPa) and the coating-to-specimen thickness ratio is small (less than $1/5$). Bending stresses have a larger effect than plane stresses: not only inducing changes in stiffness but also changes in curvature, creating a stress gradient through the coating in which the light propagates. Corrections for bending on metal specimens can be upward to 20% for thickness ratios of $1/3$. Corrections for the plane stress are smaller: typically less than 2%. For the tests presented in this investigation, the moduli ratio was 0.036 and the thickness ratio ranged between 0.16 to 0.31. As the load was bending in nature, the corresponding correction factor was 0.89 to 0.82, respectively. The stress-gradient effect through the coating is larger than the stiffening effect on the beam dynamic response. If the coating extended the length of the beam, then the increased mass and stiffness of the beam would decrease the resonant frequency by as much as 3% for the thinnest beam. Smaller application regions of the coating would further decrease this effect.

4. *Temperature Dependence*

Both PSPs and PECs are temperature dependent and can induce interference errors. The PSP temperature dependence arises from nonradiative relaxation of the excited luminophore state. This dependence is usually reflected in the Stern–Volmer calibration coefficients, A and B, as a function of temperature. For Platinum meso-tetrakis(-pentafluorophenyl) porphine-Porous Paint (PtTFPP-PP), there is a 2–4% decrease in intensity per degree Celsius, with a larger relative decrease at higher-pressure ratios. For the beam vibration test, reference and load measurements were acquired within 1°C. For the flap deflection test, the run temperature is less than the prerun reference temperature due to the expansion of the flow. Thus, as the tunnel runs, the flap temperature will decrease. The measured effect can be estimated based on oblique shock theory and an approximate surface temperature recovery factor of 0.85 assuming an adiabatic wall with the PEC acting as an insulator (while this is an oversimplified analysis, it is instructive). Based on the stagnation test conditions, at equilibrium, the surface pressure and temperature on the flap would yield a PSP intensity ratio of $I_{\text{ref}}/I = 0.28$ compared to an intensity ratio of 0.51 if the temperature were constant (remained at reference condition). Note that the stagnation pressure also decreases during the run of the blowdown tunnel at a rate of ~9 kPa/s. This too will induce an intensity change, but it is negligible (0.2% intensity rise over 0.2 s) compared to the temperature effect.

Figure 17 plots the intensity ratio with respect to time for two flap configurations. Both flaps are 4.8 mm thick and effectively exhibit no deflection during the run. Time zero is set to coincide with the start of flow over the flap. The open symbols denote the PSP directly on the flap (no PEC). The high diffusivity of the metal flap results in a slower temperature decrease and milder temperature interference. The filled symbols represent the dual-layer PSP on PEC. Because of the insulating nature of the PEC, there is a faster temperature response compared to the PSP-only flap. The temperature-affected intensity ratio decreases toward an equilibrium of ~0.24, close to the value predicted earlier in this paper. One approach to lower the temperature interference, in the absence of surface temperature measurements, is to use a reference image acquired immediately after the run is completed, before the temperature equilibrating back to the reference condition. However, this does not eliminate all temperature interference because it is also a function of pressure ratio. Another approach, in the case of high-frequency pressure and strain fluctuations compared to slower temperature drifts, is to reference the fluctuating signal to the average signal over a short period that is greater than the pressure fluctuation period but less than a significant temperature response time.

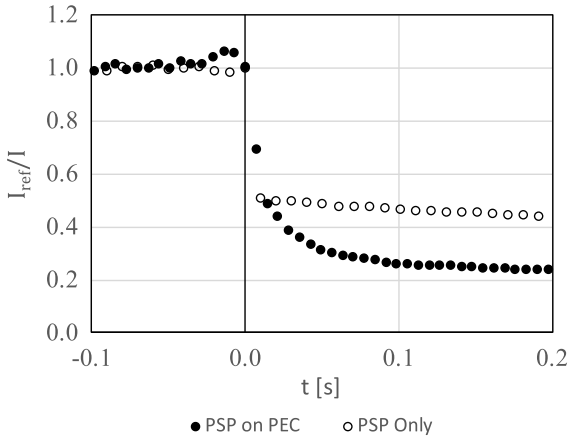

Fig. 17 Effect of temperature change on a PSP on metal and PSP/PEC-on-metal coating as flow develops on an inclined flap.

The PEC temperature dependence arises due to the glass transition nature of photoelastic coatings (typically epoxies or polycarbonates) [9,15]. The optical sensitivity K is relatively constant at temperatures below the glass transition temperature T_g. Then, as T_g is approached, the optical sensitivity rapidly decreases by 80% or greater. For the coating used in this investigation, the glass transition is $T_g \sim 170$°C and is not an issue. A second temperature effect that can arise with PECs is thermal expansion mismatch between the coating and the specimen. This is primarily an issue only near the boundaries of the coating (approximately four thicknesses), inducing thermal-induced stress.

5. *Temporal Response*

As referenced in the Introduction (Sec. I), a PSP temporal response of 20 kHz is possible using binders infused with ceramic particles. The ceramic particles can also increase the detected intensity; however, the particles can adversely affect polarization retention, decreasing the strain sensitivity. For this study, a clear polymer was used with a 90% rise time of ~2 ms as measured by the incident shockwave passage of a calibration shock tunnel at ISSI. Further testing is necessary to quantify the tradeoffs between frequency response, emission intensity (pressure resolution), and polarization retention (strain resolution).

VI. Conclusions

The theory and experimental results of a dual-layer coating with pressure-sensitive paint applied on top of a photoelastic coating are presented. A strobed dual-LED excitation approach is used: an unpolarized, blue LED excitation is used for the PSP and a circular polarized, red LED excitation is used for the PEC. The results on a vibrating cantilever beam demonstrated that both the pressure and maximum shear strain are related to the average and standard deviation, respectively, across polarization states as recorded with a digital micropolarizer camera. The pressure and strain test ranges were $20 \sim 100$ kPa_{abs} and 0–750 $\mu\varepsilon$, respectively. Frame rates were limited to 200 fps due to low image intensity relative to the full-well capacity and not the response times of the PSP and PEC. The corresponding pressure and strain uncertainty based on camera noise was 3–4%. Higher excitation energy, potentially from multiple citation sources or higher-wattage LEDs, should lower the relative camera noise and enable higher-frequency fluid–structure interaction testing and strain resolution approaching 10 microstrain. Interferences due to parasitic birefringence, specimen reinforcement, and temperature can lead to larger errors than the camera-based noise if not corrected. The technique was demonstrated on an inclined flap during the startup of a Mach 3 supersonic tunnel, demonstrating the feasibility of the technique in a high-speed transient flow.

Acknowledgments

This project is supported by National Science Foundation (NSF) and Air Force Office of Scientific Research (AFOSR) grant CBET-1802994, with Program Managers Ronald Joslin and Ivett Leyva, respectively. The authors thank Colleen Ryan, Garrett Sellers, Easton Davis, Jack Kawell, and Kimberly Lowndes for their contributions on the project. J. Kawell and K. Lowndes were supported by an NSF Research Experiences for Undergraduates (REU) Site program: EEC-1659710.

References

[1] Chism, K., Kawell, J., and Hubner, J. P., "Luminescent Measurement Technique for Analysis of Static and Dynamic Pressure and Strain Fields," AIAA Paper 2019-3150, June 2019. https://doi.org/10.2514/6.2019-3150

[2] Liu, T., and Sullivan, J. P., *Pressure and Temperature Sensitive Paints*, Springer-Verlag, Berlin, 2004.

[3] Gregory, J. W., Asia, K., Kameda, M., Liu, T., and Sullivan, J. P., "A Review of Pressure-Sensitive Paint for High Speed and Unsteady Aerodynamics," *Journal of Aerospace Engineering*, Vol. 222, No. 2, 2008, pp. 249–290. https://doi.org/10.1243/09544100 JAERO243

[4] Crafton, J., Forlines, A., Palluconi, S., Hsu, K. Y., Carter, C., and Gruber, M., "Investigation of Transverse Jet Injections in a Supersonic Cross-flow Using Fast-Responding Pressure-Sensitive Paint," *Experiments in Fluids*, Vol. 56, No. 2, 2015, Paper 27. https://doi.org/10.1007/s00348-014-1877-3

[5] Flaherty, W., Reedy, T. M., Elliott, G. S., Austin, J. M., Schmit, R. F., and Crafton, J., "Investigation of Cavity Flow Using Fast Response Pressure Sensitive Paint," *AIAA Journal*, Vol. 52, No. 11, 2014, pp. 2462–2470, https://doi.org/10.2514/1.J052864

[6] Casper, K. M., Wagner, J. L., Beresh, S. J., Spillers, R. W., and Henfling, J. F., "Study of Fluid-Structure Interactions on a Tunable Store in Complex Cavity Flow," AIAA Paper 2017-3125, June 2017. https://doi.org/10.2514/1.C035050

[7] Crafton, J., Gregory, J. W., Sellers, M. E., and Ruyten, W., "Data Processing Tools for Dynamic Pressure-Sensitive Paint," AIAA Paper 2017-0701, Jan. 2017. https://doi.org/10.2514/6.2017-0701

[8] Spottswood, S. M., Eason, T., and Beberniss, T. J., "Full-Field, Dynamic Pressure and Displacement Measurements of a Panel Excited by Shock Boundary-Layer Interaction," AIAA Paper 2013-2016, May 2013. https://doi.org/10.2514/6.2013-2016

[9] Zandman, F., Redner, S., and Dally, J. W., *Photoelastic Coatings*, Society of Experimental Stress Analysis Monograph No. 3, Iowa State Univ. Press, Ames, IA, 1977.

[10] Dally, J., "An Introduction to Dynamic Photoelasticity," *Experimental Mechanics*, Vol. 20, No. 12, 1980, pp. 409–416. https://doi.org/10.1007/BF02320881

[11] Lesniak, J. R., and Zickel, M. J., "Applications of Automated Grey-Field Polariscope," *Proceedings of the Society of Experimental Mechanics Conference on Experimental and Applied Mechanics*, Soc. of Experimental Mechanics, Bethel, Connecticut, June 1998, pp. 298–301.

[12] Hubner, J. P., Chen, L., Liu, Y., Schanze, K., Nicolosi, J., Ifju, P., and El-Ratal, W., "Characterization of a New Luminescent Photoelastic Coating," *Experimental Mechanics*, Vol. 45, No. 2, 2005, pp. 137–143. https://doi.org/10.1007/BF02428186

[13] Esirgemez, E., and Hubner, J. P., "Luminescent Photoelastic Coating Image Analysis and Strain Separation on a Three-Dimensional Grid," *Optical Engineering*, Vol. 49, No. 8, 2010, Paper 083601. https://doi.org/10.1117/1.3475946

[14] Hua, S. Q., and Luo, Y., "Improvement of the Coating Formulation in Luminescent Photoelastic Coating Method," *Experimental Techniques*, Vol. 37, No. 4, 2013, pp. 19–24. https://doi.org/10.1111/j.1747-1567.2011.00721.x

[15] "Corrections to Photoelastic Coating Fringe-Order Measurements," Micro-Measurements, TN-706-1, Rayleigh, NC, Aug. 2015.

[16] Zecchino, M., *PolarView™ User Manual*, Rev. 2.3.0.0 A, 4D Technology Corp., Tucson, AZ, June 2017.

[17] Hegde, A., Sellers, G., Ölçmen, S., and Hubner, J.P., "Pressure and Strain Measurement on an Inclined Flap in Supersonic Flow Using a Dual-Layer Luminescent Coating," AIAA Paper 2020-2969, June 2020. https://doi.org/10.2514/6.2020-2969

L. Ukeiley
Associate Editor